Zweitveröffentlichung/ Secondary Publication

b

Staats– und
Universitätsbibliothek
Bremen

Peng Xiao, Yu-hai Lu, Yi-zhong Liu, Zhuan Li, Hua-chan Fang, Wei Zhou, Renato S. M. Almeida, Yang Li

[+]

Microstructure and properties of Cu-Ti alloy infiltrated chopped Cf reinforced ceramics composites

Microstructure and properties of Cu-Ti alloy infiltrated chopped C_f reinforced ceramics composites

Peng Xiao[a], Yu-hai Lu[a], Yi-zhong Liu[a], Zhuan Li[a], Hua-chan Fang[a], Wei Zhou[a],
Renato S.M. Almeida[b], Yang Li[a],*

[a] *State Key Laboratory of Powder Metallurgy, Central South University, Changsha 410083, PR China*
[b] *Advanced Ceramics, University of Bremen, Bremen 28359, Germany*

ABSTRACT

Keywords:
Chopped fibers architecture
Microstructure
Tribological property
Cu-Ti alloy
Reactive melt infiltration

Novel friction composites (C/C-Cu_5Si-TiC) were prepared via reactive melt infiltration (RMI) of Cu-Ti alloy into porous C/C-SiC composites. The microstructure, physical properties and tribological behaviors of the novel material were studied. Results were compared to conventional C/C-SiC composites produced by liquid silicon infiltration(LSI). The resultant composite showed the microstructure composed of Cu_5Si matrix reinforced with TiC particles and intact C/C structures. Most importantly, the composite did not present traces of free Si. As a result, the C/C-Cu_5Si-TiC composite showed higher flexural strength, impact toughness and thermal diffusivity in comparison to C/C-SiC composites. Tribological properties were measured using 30CrSiMoVA as a counterpart. In general, the C/C-Cu_5Si-TiC composites showed lower coefficient of friction(COF), but higher wear resistance and frictional stability. The improved wear resistance of the C/C-Cu_5Si-TiC composites is credited to the formation of friction films from Cu_5Si matrix. Other deformation and wear mechanisms are also described considering the microstructural observations.

1. Introduction

Since the 1990s, C/C-SiC composite derived from liquid silicon infiltration (LSI) method has been gradually developed due to their favorable mechanical property aligned with relatively low cost and high level of reproduction [1,2]. Furthermore, LSI based C/C-SiC composites are known to be a good option for friction materials due to their COF, high-temperature resistance, damage tolerance and insensitivity to the braking environments [3–7]. Therefore, current C/C-SiC composites are commonly applied for high-performance braking system for sports cars, luxury sedans, elevators [6–8]. Additionally, previous investigations indicated that the C/C-SiC composite was one of the best candidates for applications in high-speed train, aircraft, armored vehicle, engineering machinery and some other heavy-duty brake systems [9,10]. However, the braking tests revealed that the wear rate of C/C-SiC composites was relatively high, and their COF at different brake speeds was not stable. These aspects are related to the presence of free Si phase, complex fiber architectures and inhomogeneous phase distributions, etc. [11–13].

In order to improve the mechanical, thermal and tribological properties of C/C-SiC composites, many investigations have studied the infiltration of silicon-based alloys into porous C/C [14–16]. Investigations regarding to Si-Mo, Si-Al, Si-Nb, Si-Mo-Ti and Si-Zr alloys

modified C/C-SiC composites indicated that these silicon-based alloys could effectively improve the mechanical performances, as well as oxidation resistance and ablation resistance at elevated temperatures [17–21]. However, less attention was paid to the tribological behavior of the above-mentioned Si-alloy modified ceramic composites. Fan et al. investigated the microstructure and physical properties of Ti_3SiC_2 modified C/C-SiC composites prepared by employing TiC slurry infiltration and LSI process [22,23]. The experimental results indicated an improved friction stability, increase of mechanical strength as well as a lower wear rate for the Ti_3SiC_2 modified C/C-SiC composites. Similar results were achieved with the Fe-Si modified C/C-SiC composites [15]. In both cases, the improvement was related to the decrease of residual Si content. Our previous investigations on Cu_3Si modified C/C-SiC composites revealed that the mass fraction of residual Si, wear rate under low braking speed as well as micro-harness were concurrently decreased in comparison to that of C/C-SiC composites [24]. However, it was perceived that residual Si could not be completely removed via RMI of silicon based alloy. Therefore, it can be assumed that the tribological properties of C/C-SiC composites can be further enhanced with Si-free alloys. In this sense, Cu-Ti alloy could be a good alternative since it presents favorable wetting to carbon and SiC. Hence, Ti could react with carbon and SiC [25], while copper could also easily react

with the free Si to form Cu-Si alloy phases [26].

In this work, LSI-based C/C-SiC preforms were infiltrated with Cu-Ti alloy via reactive-melt infiltration process. The main purpose was to eliminate the residual silicon and simultaneously improve the mechanical and tribological properties for C/C-SiC composites. Experimentally, the microstructure, mechanical and thermal properties of C/C-SiC composites infiltrated by Cu-Ti alloy (C/C-Cu$_5$Si-TiC) were characterized and compared to C/C-SiC composites, in order to evaluate the new composite system. Moreover, the tribological behaviors of both materials under different speeds were comparatively investigated using 30CrSiMoVA as a counterpart.

2. Material and method

2.1. Fabrication of the composites

Polyacrylonitrile (PAN) based carbon fibers (T700, filament of 12 K, Toray) were used as raw material for the chopped fiber web preforms. For the matrix, commercially available Si, Ti and Cu powders with mean particle sizes of 30–50 μm and purity of 99.0% were used in LSI and RMI processes.

The fabrication steps of the C/C-SiC and C/C-Cu$_5$Si-TiC composites are schematized in Fig. 1. The first step for both composites was the production of a porous C/C composite. For that, the short fiber webs were repeatedly stacked and then needle-punched. The needle punching density was 15–35 pins cm^{-2}, and the layer density and bulk density of the chopped fiber fabric preform was approximately 12–15 layers cm^{-1} and 0.18 g cm^{-3}, respectively. Afterwards, porous C/C composites were produced via chemical vapor infiltration (CVI) process at 1000 °C for 120 h in argon atmosphere with absolute pressure of 0.1 MPa. Commercial C$_3$H$_6$ gas was applied as a precursor, and H$_2$ as a carrier and diluting gas (C$_3$H$_6$/H$_2$ = 10 ml min^{-1}, H$_2$ = 20 ml min^{-1}). Finally, a regular LSI process and combined process of LSI and RMI were performed on the porous C/C composites to prepare the C/C-SiC composites and C/C-Cu$_5$Si-TiC composites, respectively. The "standard" LSI process was conducted at 1750 °C with 1 h dwell time under vacuum conditions (< 1 kPa). Concerning the combined process, the LSI process was firstly conducted at 1750 °C under vacuum condition for merely 0.5 h to achieve porous C/C-SiC composites. Subsequently, the as-prepared C/C-SiC composites were infiltrated by RMI at 1300 °C with 2 h dwell time in vacuum (absolutely pressure < 1 Pa). Note that uniformly mixed Cu and Ti powders with the mass ratio of Cu/Ti = 90/10 were applied for the RMI process in this work.

2.2. Analysis methods

For a correct interpretation of the tribological behavior, the as-prepared composites here were firstly characterized in regard to general properties: density/porosity,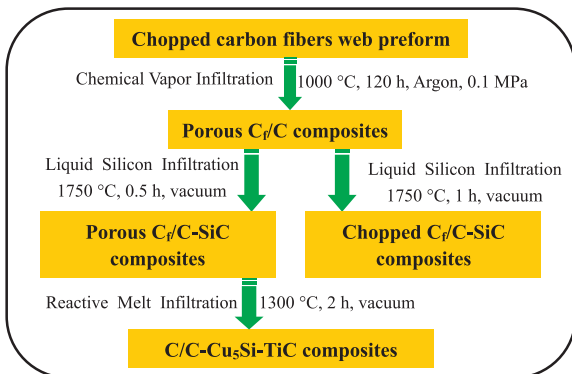 microstructure, crystal phases, mechanical properties and thermal diffusion. The bulk density and open porosity of samples were measured by Archimedes' method using distilled water according to DIN EN 1389. The phases in samples were analyzed by X-ray diffraction (XRD, Rigaku D/max 2550 PC) using nickel-filtered Cu Kα radiation. The microstructure, as well as the morphology of the worn surfaces and wear debris were observed by scanning electron microscopy (SEM, FEI Nova NanoSEM-230) equipped with a Link energy-dispersive X-Ray analyzer (EDX), and a three-dimensional rotational digital video microscope (HIROX KH-7700, Japan).

The mechanical tests were conducted on an Instron 1196 universal test machine. Different sample geometries were prepared by water-cutting. For each type of test, a minimum of seven specimens were measured for statistical purpose.

Flexural strength (σ$_f$) was evaluated by three-point-bending tests with a span/thickness ratio of 10. The loading rate for the mechanical tests in this work was set to 1 mm/min. The impact toughness tests were performed on specimens with the geometry of 55 mm × 10 mm × 10 mm, according to Chinese Standard GB/T14389-93. Furthermore, the micro-hardness of each phase in the as-prepared composites was measured by the nano-indentation method using nano-indentation apparatus (CSMUNHT) with a Berkovich-type-pyramid shape diamond indenter. The micro-hardness values were calculated by following the Eq. (2.1):

$$HV = \frac{2p \sin \frac{136°}{2}}{d^2} = \frac{1.8544p}{d^2} \tag{2.1}$$

where P is the contact load (N) and d is the length of the diagonal of the indentation surface (mm). All measurements were carried out with a load of 200 mN and a contact time of 25 s at room temperature. In total, ten measurements were done for each phase on a polished perpendicular section.

The thermal diffusivity of the samples was measured by a laser flash apparatus (Netzsch LFA427, Germany) with the sample size of Φ12.7 mm × 2 mm under room temperature in argon atmosphere.

2.3. Tribological test

The braking tests were conducted on a laboratory-scaled disk-on-disk MM-1000 dynamometer (Xi'an Shuntong Technical Institute, China). Detailed information of the testing machine was previously reported in Ref. [13]. Preselected parameters used for braking tests were listed in Table 1. During the braking tests, the composites samples acted as stator, while the 30CrSiMoVA alloy steel acted as rotor. The geometry of the specimen was 75 mm in out-diameter, 53 mm in inner-diameter and 15 mm in thickness. During the braking tests, the rotating velocity, brake moment, and brake time were recorded. Afterwards, COF was calculated automatically by the computer. The linear wear rate was calculated considering the thickness difference of the disk before and after the braking tests divided by the number of braking times.

The above test was repeated 20 times in this work.

3. Results and discussion

3.1. Microstructure and phase analysis

A summary of the open porosity and bulk density of the as-prepared composites is listed in Table 2. As it can be seen, the open porosity of C/C composites is significantly decreased after the subsequent infiltrations of liquid Si or Cu-Ti alloy. With the final LSI or RMI step, both composites show a low open porosity of around 6%, although a difference in bulk density is seen due to the different compositions: bulk density of the C/C-Cu$_5$Si-TiC composite ranging from 3.53 to 3.66 g cm^{-3} and C/C-SiC composite ranging from 2.0 to 2.1 g cm^{-3}.

Fig. 2 presents the XRD patterns for the porous C/C-SiC,

Fig. 1. Schematic illustration of the manufacturing process for the C/C-SiC and C/C-Cu$_5$Si-TiC composites.

Table 1
Preselected parameters for braking tests.

Composites	Mating materials	Braking speed (m/s)			Repeated times	Inertia (kg m^2)	Braking pressure (MPa)
C/C-Cu$_5$Si-TiC	30CrSiMoVA alloy steel	10	15	20	20	0.1	1.0
C/C-SiC		10	15	20	20	0.1	1.0

Table 2
Open porosity and bulk density for C/C, C/C-SiC and C/C-Cu$_5$Si-TiC composites.

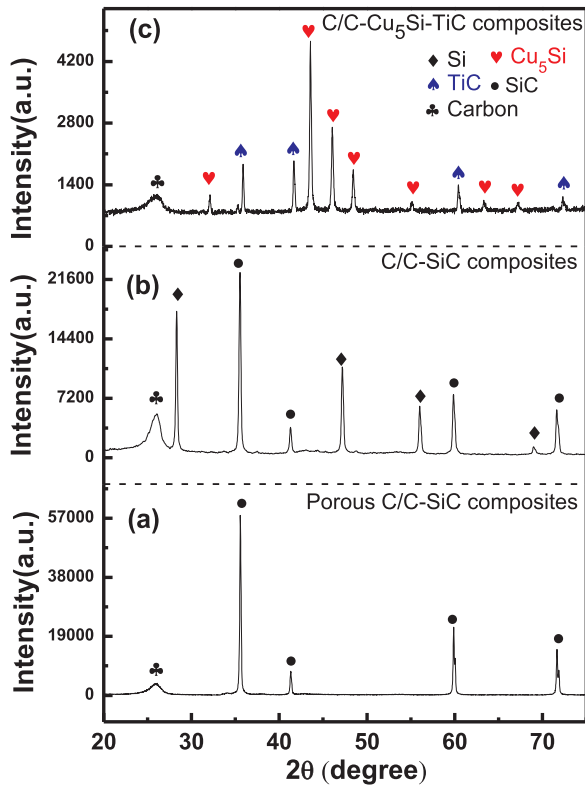| Materials	Bulk density/(g cm^{-3})	Open porosity/%
Porous C/C	1.20	37.7
Porous C/C-SiC	1.45–1.55	26.7
C/C-Cu$_5$Si-TiC	3.53–3.66	5.8–6.2
C/C-SiC	2.0–2.1	5.5–6.3

Fig. 2. XRD patterns for the as-prepared composites.

Table 3
Compositions of the C/C-SiC and C/C-Cu$_5$Si-TiC specimens.

Composites	C (wt%)	Si (wt%)	SiC (wt%)	Cu$_5$Si (wt%)	TiC (wt%)
C/C-SiC	15.2	31.5	53.3	0	0
C/C-Cu$_5$Si-TiC	23.4	0	2.1	53.5	21

conventional C/C-SiC and C/C-Cu$_5$Si-TiC composites. The quantification of these results are shown in Table 3 as the crystal phase compositions. As shown in Fig. 2(a), the porous C/C-SiC composites before RMI process are composed of carbon and SiC without traces of free Si. However, the conventional LSI process leads to the formation of a high content (31.5 wt%) of free silicon (see Fig. 2(b)) in the C/C-SiC composites. As shown in Fig. 2(c), the formed composite after RMI presents two new phases, 53.5 wt% of Cu$_5$Si and 21.0 wt% of TiC, but a much lower content of SiC, 2.1 wt%. Possible reactions that can happen during RMI are discussed below together with the microstructural

observations.

The SEM images of the porous C/C composites before LSI are shown in Fig. 3. The CVI process leads to a highly porous C/C microstructure, in accordance to the porosity measurements (see Fig. 3(a)). It can also be observed that the porous structure is rather heterogeneous, i.e., great variety of pore sizes that are unevenly distributed along the microstructure of the composite. Fig. 3(b) shows a higher magnification picture, in which it can be observed that the carbon fiber is well coated by a pyrolytic carbon (PyC) layer, thickness of 10–15 μm, formed by the CVI process. Here it is important to highlight that these typical C$_f$/PyC units will protect the fiber from the aggressiveness of the liquid silicon or molten alloy during LSI and/or RMI processes.

Fig. 4 shows the SEM morphology of the C/C-SiC composites. As shown in Fig. 4(a), the C/C-SiC composites are quite dense with merely a few pores, corresponding well to the open porosities listed in Table 2. During LSI, the liquid Si infiltrates the highly porous C/C structure due to capillary force, and small pores are preferentially filled. As a results, SiC (gray phase) is formed within the small pores while the big pores get filled with residual Si (light gray phase). Due to the broad distribution of the pores in the porous C/C composites, the free Si in the as-prepared C/C-SiC composites is also not evenly distributed. Fig. 4(b) displays the typical morphology of a C/C segment surrounded by SiC/Si matrix. The PyC layers surrounding the fibers inevitably react with the liquid silicon and result in formation of SiC layers. However, the inner parts of the C/C segment are seemingly well-protected, because the liquid Si could not fully diffuse through the developed SiC layer and react with the inner carbon fiber in the given infiltration time [27].

Fig. 5 displays the SEM morphology of the porous C/C-SiC composites before RMI. As shown in Fig. 5(a), the porous C/C is coated with SiC layer (gray in figure) due to the excellent wet ability between the liquid silicon and the C/C. Additionally, the majority of pores in the C/C composites are retained in the porous C/C-SiC composites, corresponding well to the open porosity listed in Table 2. Most importantly, the SiC layer could improve the wetting ability between the carbon and copper alloy. After such special LSI process, the C$_f$/C segment is also unavoidably aggressed by liquid silicon. As a result, SiC layer with thickness of 7–10 μm around the C$_f$/C segment (see Fig. 5(b)) is formed. However, the majority of C$_f$/C segments in the porous C/C-SiC are still free of liquid silicon aggressiveness. Therefore, it is reasonable to infer favorable mechanical properties in the resulting C/C-Cu$_5$Si-TiC composites.

Fig. 6 shows the SEM morphologies and elemental analysis results of the C/C-Cu$_5$Si-TiC composites. Clearly, the porous C/C-SiC composites shown in Fig. 5(a) are completely infiltrated without obvious macro pores after RMI (see Fig. 6(a)). This confirms that Cu-Ti melt shows good wettability to the SiC layers formed around the carbon phase. A typical unit of C$_f$/PyC/alloy matrix is presented in Fig. 6(b). The C$_f$ is still well coated by the PyC, while the dense SiC and TiC layers appear to be particle-stack structures in the C/C-Cu$_5$Si-TiC composites. Moreover, fine particles are also observed along the formed alloy matrix especially in the areas close to the PyC layers. In order to fully understand the distribution of the ceramic phases within such unit, the EDX was used to investigate the element distributions. Fig. 6(c)–(f) present the C, Ti, Si and Cu distributions in Fig. 6(b), respectively. Carbon is distributed within the region of the C$_f$/PyC unit. Ti is found mainly in the region around the PyC and within the micro-particles. In contrast, Cu and Si are uniformly distributed along the matrix (see Fig. 6(e) and (f)). Based on the results of Fig. 6(c)–(f) and the XRD patterns in
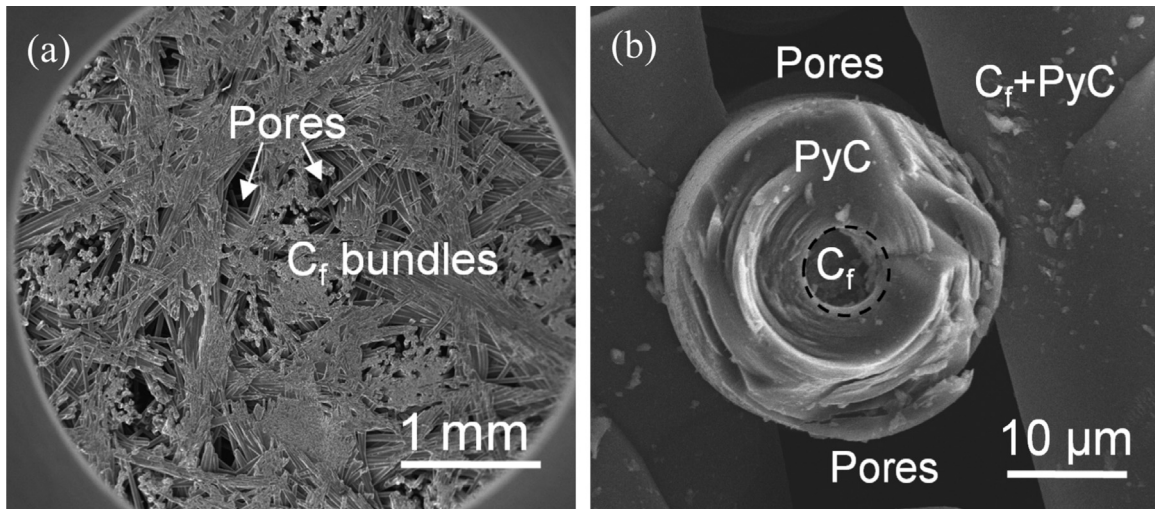
Fig. 3. SEM morphology of the porous chopped C_f/C (a) and higher magnification showing a typical C_f/PyC unit (b).
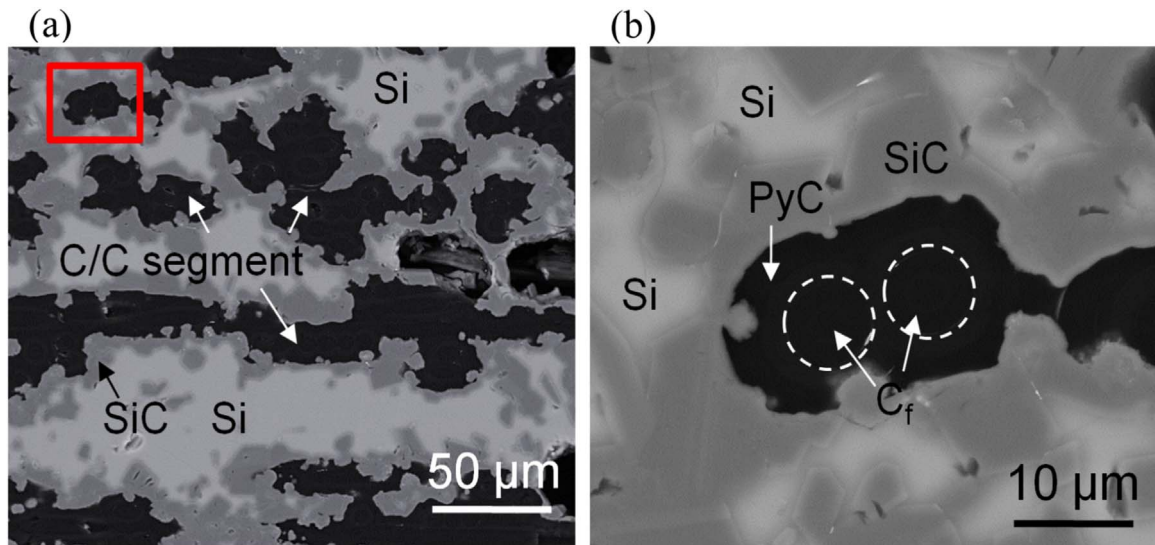

Fig. 4. SEM morphology of the C/C-SiC composites (a) and higher magnification of red-lined region (b). (For interpretation of the references to color in this figure legend, the reader is referred to the web version of this article.)

Fig. 5. SEM morphology of the porous C/C-SiC before RMI (a) and higher magnification of red-lined region (b). (For interpretation of the references to color in this figure legend, the reader is referred to the web version of this article.)
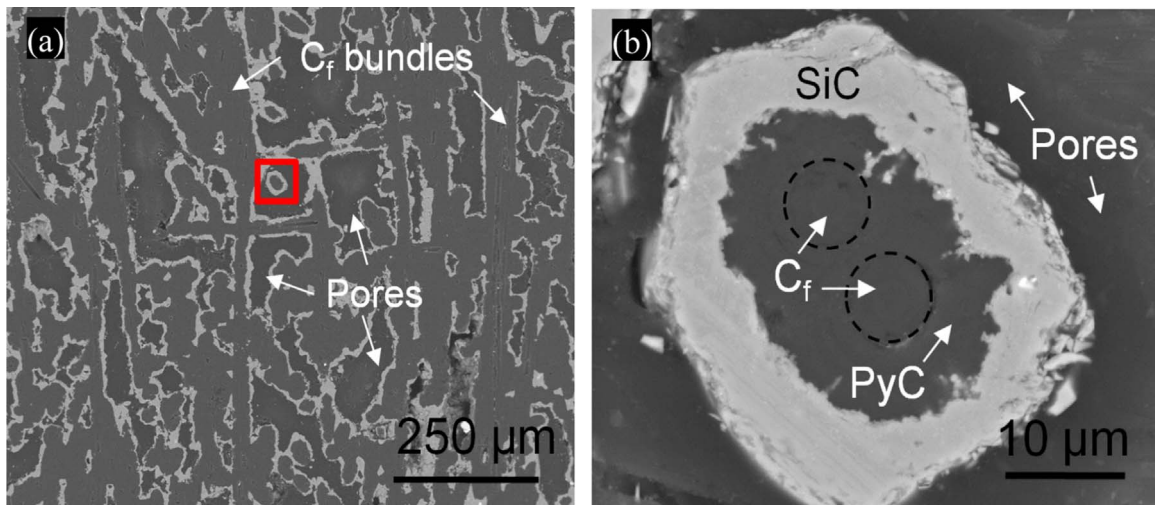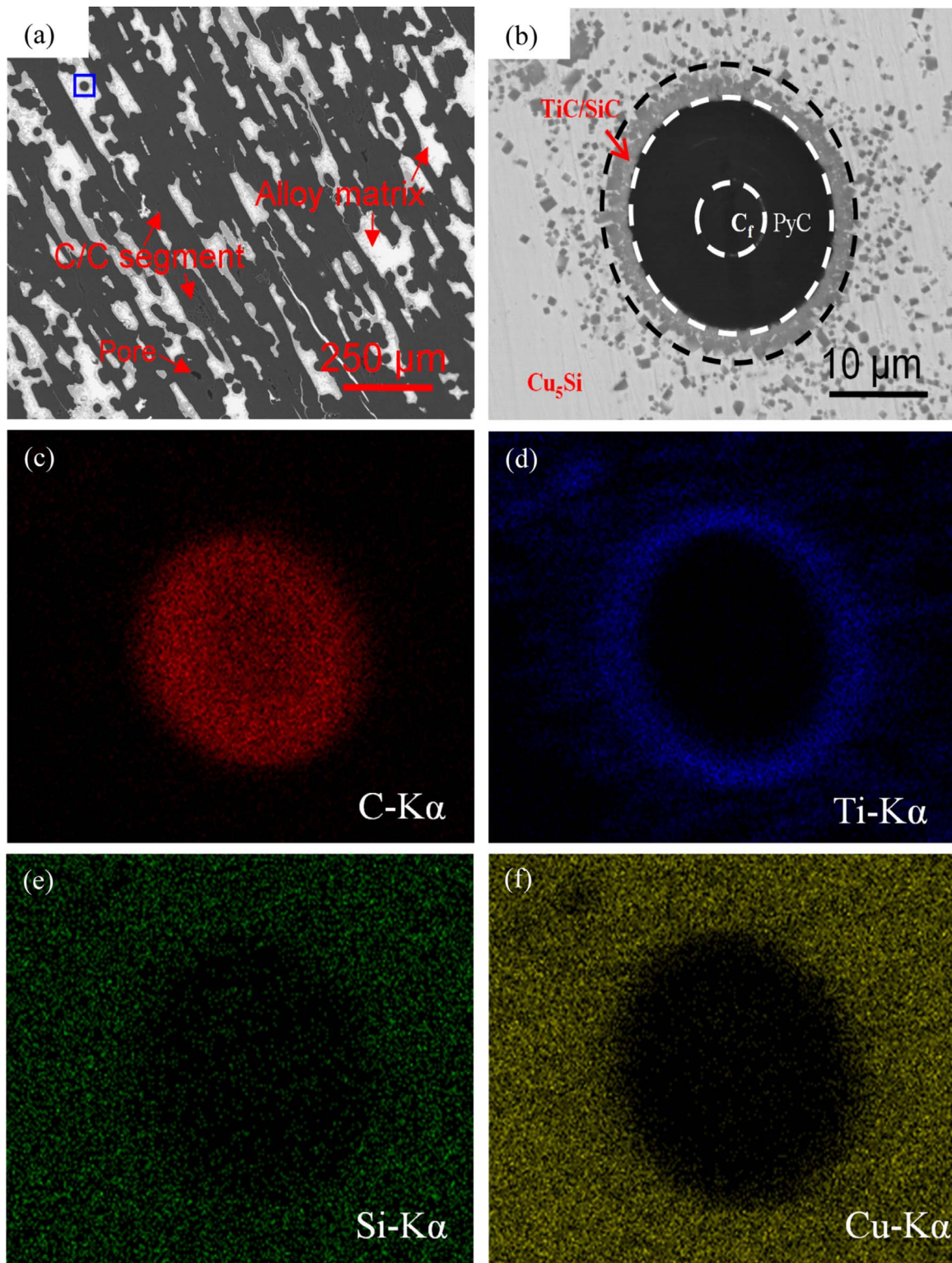
Fig. 6. SEM morphology of the C/C-Cu$_5$Si-TiC composites (a), higher magnification showing a typical C/PyC unit (b), C distribution (c), Ti distribution (d), Si distribution (e) and Cu distribution (f).

Table 4
Vickers micro-hardness of some phases in C/C-SiC and C/C-Cu$_5$Si-TiC composites.

Composition	Cu$_5$Si	β-SiC	TiC	Si
Average value of HV$_m$	150	2410	1619	1183

Fig. 2(c), it could be deduced that the dark gray phase is composed mainly of TiC with traces of SiC, while the light gray phase in Fig. 6(b) is presumably Cu$_5$Si.

The distributions of TiC, SiC and Cu$_5$Si phases in the matrix involve a series of chemical reaction under the given infiltration conditions. As it is well-known, the contact angle between Cu and SiC is about 165°, indicating poor wetting between Cu and SiC [28]. Whereas, the Si could

Sample	3-point flexural strength/MPa ⊥	Thermal diffusivity/ cm^2 s^{-1} ⊥	Impact toughness/ kJ m^{-2} ⊥
C/C-SiC	96 ± 22	0.05	2.8 ± 0.7
C/C-Cu$_5$Si-TiC	110 ± 37	0.08	7.9 ± 1.5

"⊥" was defined as the load (or heat fluid) directions perpendicular to the surface of the chopped carbon fiber web(namely the friction surface).

easily react with Cu to form Cu-Si alloy at a low temperature [28]. Moreover, Ti shows good wettability to SiC, and the liquid Ti can react with SiC at elevated temperature. In the present case, liquid Cu$_2$Ti is formed when the process temperature is higher than 875 °C, according to the Cu-Ti binary phase diagram [29]. Therefore, it can be expected that the Ti species in formed liquid Cu$_2$Ti will react firstly with the SiC layer around PyC forming TiC and Si. Subsequently, the Cu element in the liquid reacts with the free Si to form Cu$_5$Si. Hence, TiC is formed around the C$_f$/PyC unit, while Cu$_5$Si develops along the former porous structure of the C/C-SiC composite. According to Table 3, it could be deduced that these reactions will take place until most of the SiC in the porous C/C-SiC is consumed. Furthermore, liquid Cu$_2$Ti probably reacts with PyC to form TiC in the SiC-poor regions. Therefore, the generated

TiC phase and residual SiC phase in Fig. 6(b) are mainly observed in the region around the PyC layers. The possible chemical reactions during infiltration of Cu-Ti alloy into porous C/C-SiC composites are summarized in equations as follows.

$$Ti + SiC \rightarrow TiC + Si \tag{3.1}$$

$$Cu + Si \rightarrow Cu_5Si \tag{3.2}$$

$$Ti + C \rightarrow TiC \tag{3.3}$$

3.2. Mechanical and thermal properties

Generally, the tribological characteristics, for instance, the COF and wear rate, are related to the hardness of the phases in the frictional composites [30,31]. In order to estimate the hardness of the composites, Vickers micro-hardness (HV$_m$) measurement were performed on the different matrix phases of the composites. The experimental results of the HV$_m$ are summarized in Table 4. Clearly, SiC phase shows the highest results (mean value of 2410), while the Cu$_5$Si is the softest phase in the matrix. Considering the phase composition of each composite, it can be deduced that C/C-Cu$_5$Si-TiC composites are significantly softer than the C/C-SiC composites. Nevertheless, here it is important to highlight that the C/C-Cu$_5$Si-TiC composite shows rather new and interesting reinforcement system. From the microstructural
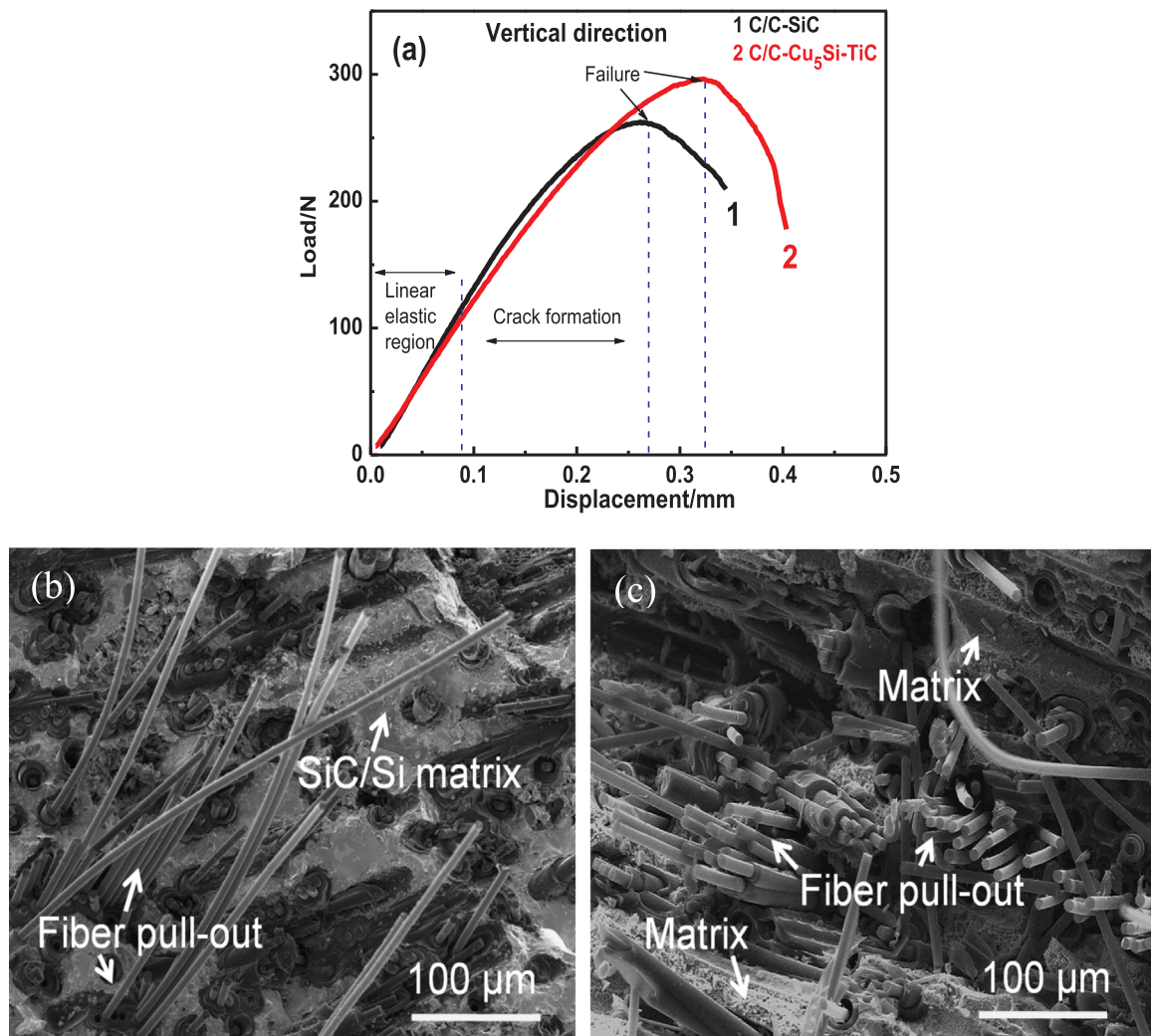

Fig. 7. Flexural property of C/C-SiC and C/C-Cu5Si-TiC specimens (a) load-displacement curves for C/C-SiC and C/C-Cu$_5$Si-TiC, (b) fractured surface of C/C-SiC specimen, (c) fractured surface of C/C-Cu$_5$Si-TiC specimen.
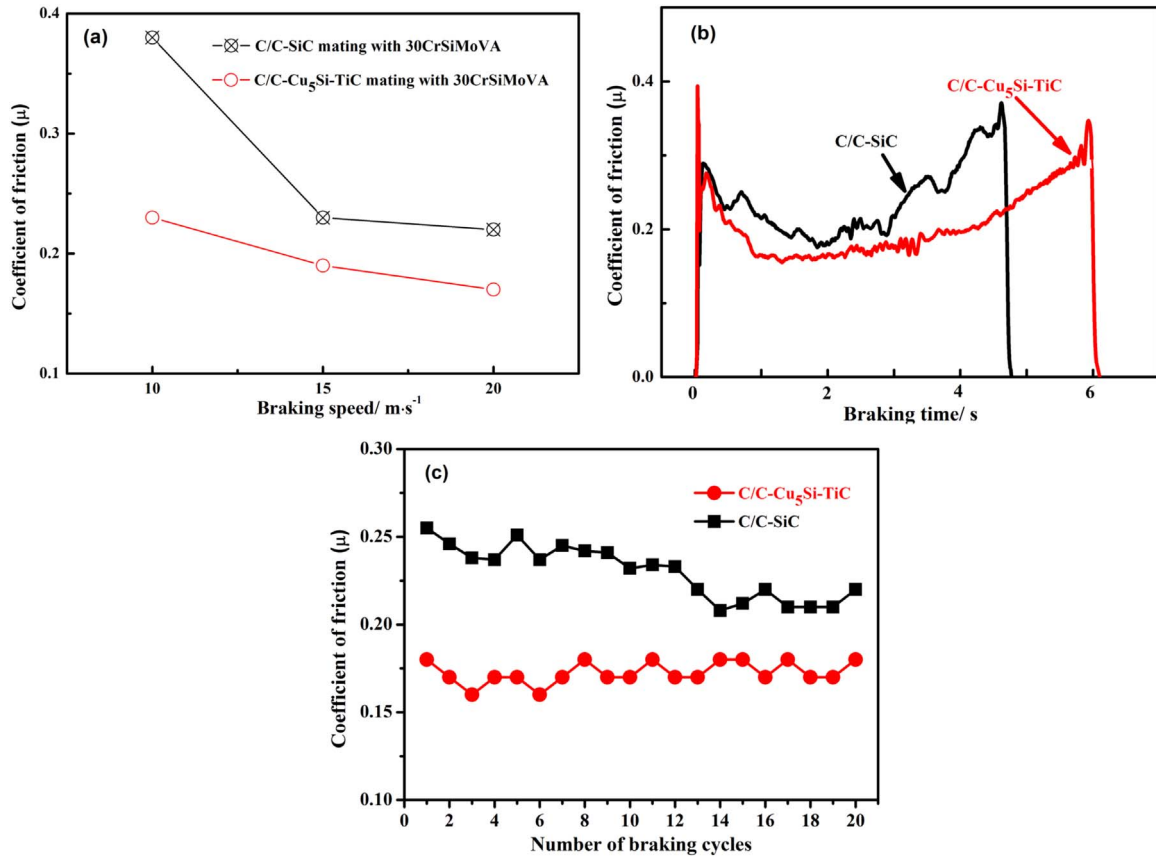
Fig. 8. (a) Average COF for the C/C-SiC and C/C-Cu$_5$Si-TiC composites under different braking speeds, (b) typical brake curve of the C/C-SiC and C/C-Cu$_5$Si-TiC composites under braking speed of 20 m/s, (c) COF evolution during 20 cycles of braking tests at an initial braking speed of 20 m/s.
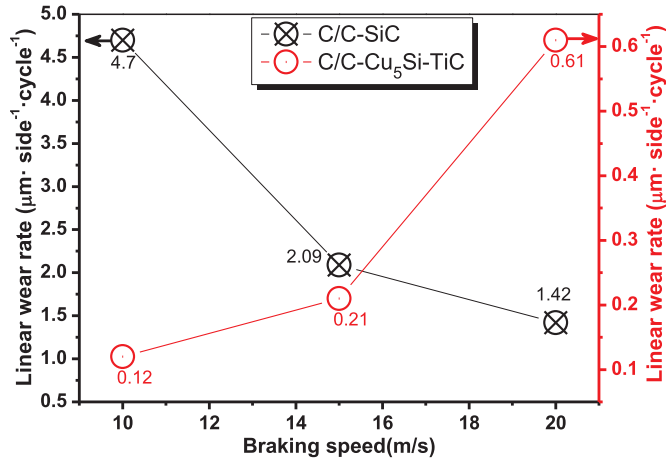

Fig. 9. Linear wear rate with braking speed of the C/C-SiC and C/C-Cu$_5$Si-TiC composites.

analysis of Fig. 6, it can be seen that the soft Cu$_5$Si matrix is reinforced, at the same time, by well-dispersed TiC micro-particles and the randomly distributed C/PyC segments.

In order to get an overview of the as-prepared composites, the flexural strength, impact toughness and thermal diffusivity of the as-prepared C/C-SiC and C/C-Cu$_5$Si-TiC composites are listed in Table 5. Compared to C/C-SiC composites, the impact toughness, thermal diffusivity and flexural strength of C/C-Cu$_5$Si-TiC composites are increased to 7.9 ± 1.5 kJ m^{-2}, 0.08 cm^2 s^{-1} and 110 ± 37 MPa, respectively. As shown in Table 4, Cu$_5$Si is much softer than Si and SiC phases. Therefore, it could be induced that Cu$_5$Si as matrix subjected to impact loads could deform larger, and absorb more energy than Si and SiC

phases, resulting higher impact toughness. Moreover, Cu$_5$Si also shows higher thermal conductivity than that of Si and SiC, corresponding to an improved thermal diffusivity in C/C-Cu$_5$Si-TiC composites.

Fig. 7 presents the load-displacement curves under flexural stress and fractured surface morphologies for C/C-SiC and C/C-Cu$_5$Si-TiC composites. As shown in Fig. 7(a), both composites show the pseudo-plastic behavior desired for CMCs. Linear elastic deformation can be observed until the load reaches approximately 25% of the maximum load. Further loading results in a non-linear continuous progression because of the matrix crack formation and propagation. After reaching maximum load, a rapid decrease of load is observed, signaling irreversible failure. The main difference between both composites is the maximum load achieved. Further differences can be seen on the fracture surfaces shown in Fig. 7(b) and (c). As previously mentioned, the fracture starts on the matrix and fiber pull-out is observed for both composites. Nevertheless, the matrix fracture of the C/C-SiC composites (see Fig. 7(b)) is much more planar. In addition, several C$_f$/PyC units also failed in the same plane as the matrix, presumably because of the higher interaction due to the aggressiveness of the liquid silicon. In contrast, the surface shown in Fig. 7(c) for the C/C-Cu$_5$Si-TiC composite is much rougher, and both fibers and PyC units seem to be pull-out. As seen in the microstructural analysis of Fig. 7, the C/C-Cu$_5$Si-TiC composites have a rather complex reinforcement system. The soft Cu$_5$Si matrix contains several TiC particles, at which deflection of the initial cracks can already occur. As the loading progressing, the C$_f$/PyC units can most likely debond from the matrix. The final failure will only occur after most of the load-carrying fibers fail. As a consequence of these different crack deflection mechanisms, the C/C-Cu$_5$Si-TiC composites ended up showing a slightly higher flexural strength.
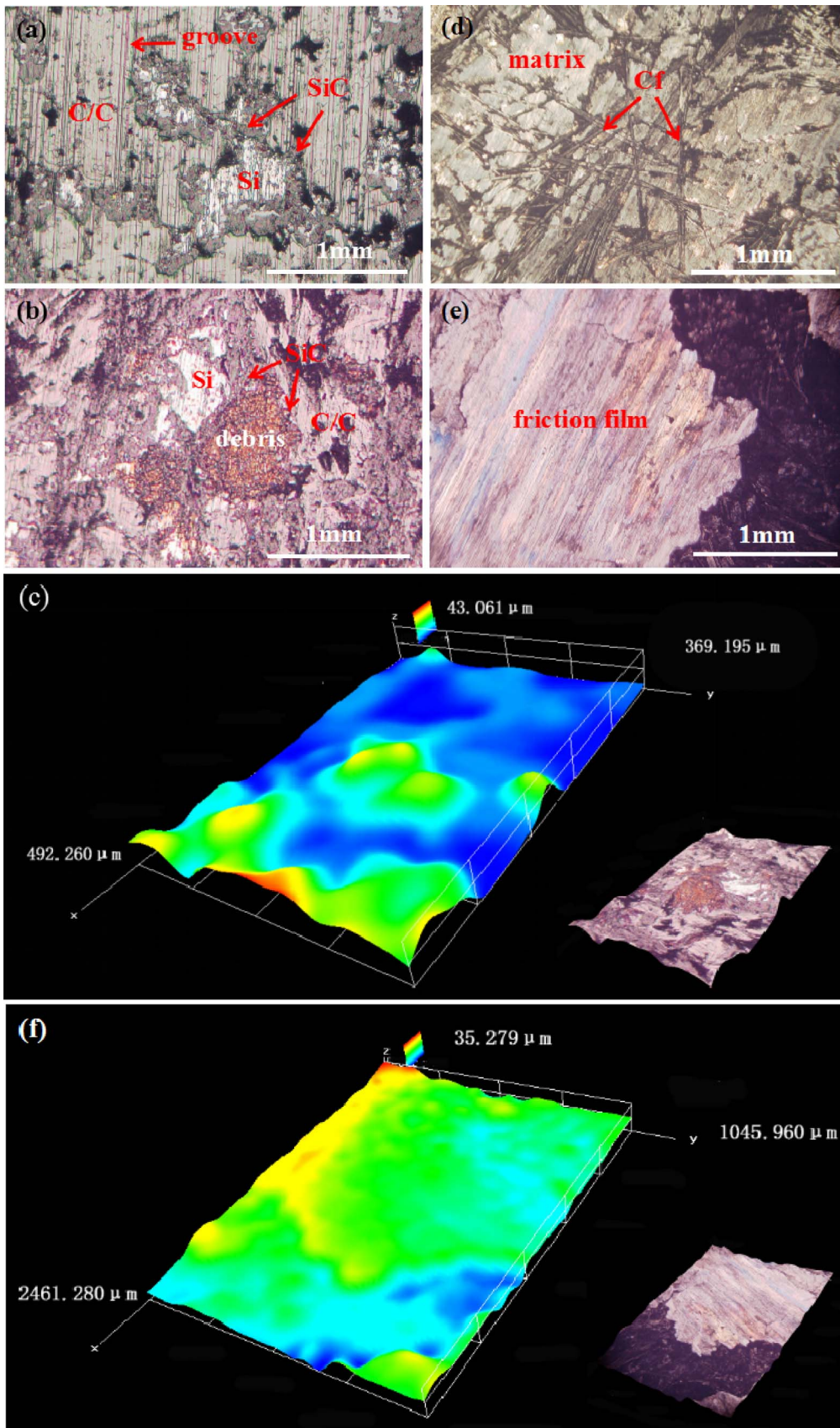
Fig. 10. Microscopic morphology of friction surface of the composites after braking at 20 m/s. (a) C/C-SiC specimen after the 1st brake cycle, (b) C/C-SiC specimen after the 20th brake cycle, (c) 3D morphology of C/C-SiC composites after the 20th brake cycle, (d) C/C-Cu$_5$Si-TiC specimen after the 1st brake cycle (e) C/C-Cu$_5$Si-TiC specimen after the 20th brake cycle; (f) 3D morphology of C/C-Cu$_5$Si-TiC composites after the 20th brake cycle.
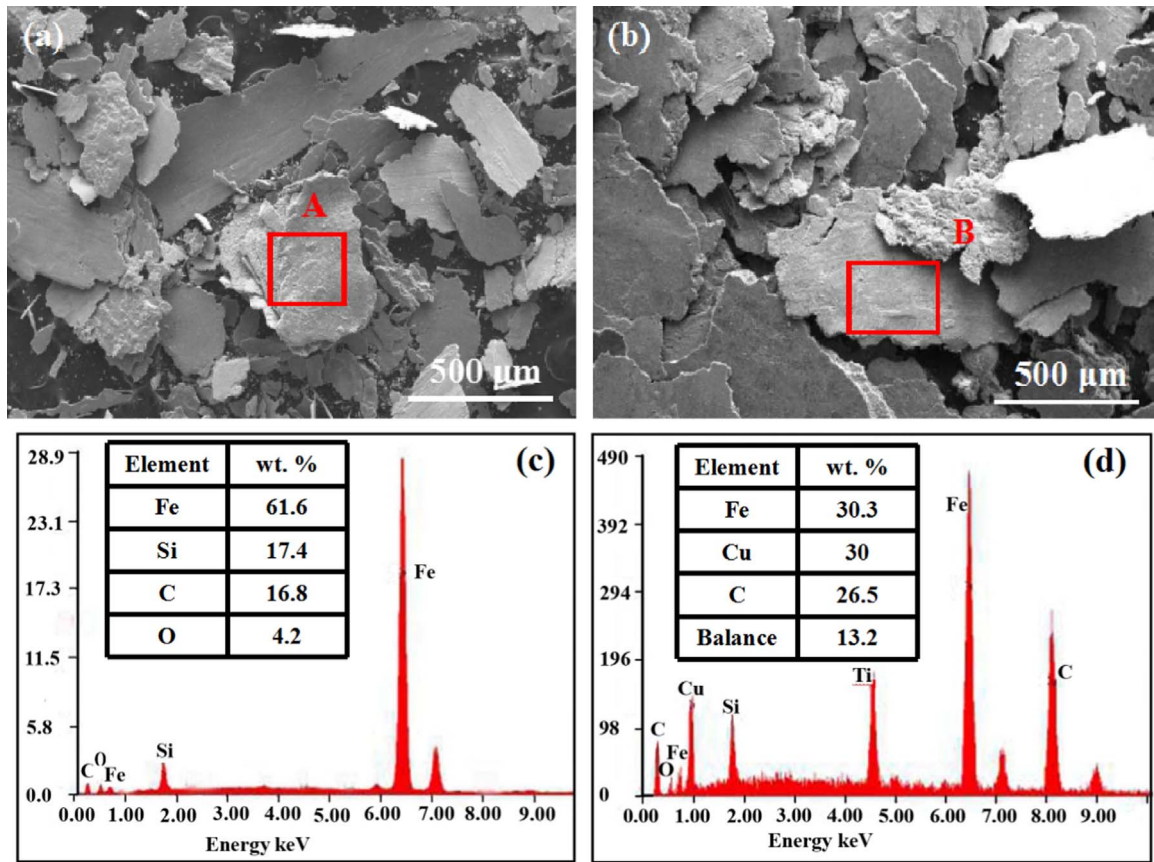
Fig. 11. SEM micrographs of wear debris: (a) C/C-SiC composite; (b) C/C-Cu$_5$Si-TiC composite; (c) EDS of highlighted region A; (d) EDS of highlighted region B.

3.3. Tribological behaviors

The main results of the tribological tests are presented in Figs. 8 and 9. Fig. 8(a) shows the COF for different braking speeds using C/C-SiC and C/C-Cu$_5$Si-TiC composites mating with 30CrSiMoVA steel counterpart. In the present case, the COF of the C/C-Cu$_5$Si-TiC composites is, in general, lower than that of C/C-SiC composites. Additionally, the COF of both composites specimens decrease with increasing braking speed. However, the COF of the C/C-Cu$_5$Si-TiC composites is somewhat less sensitive to the applied friction speed. Typical brake curves of these two specimens tested at braking speed of 20 m/s are presented in Fig. 8(b). The brake curves with similar shape of horse saddles are observed in both specimens. However, a smoother curve is obtained in C/C-Cu$_5$Si-TiC specimens, indicating a more stable braking process. Fig. 8(c) presents the evolution of COF during 20 braking cycles for C/C-SiC and C/C-Cu$_5$Si-TiC composites. Clearly, the COF of C/C-SiC composites fluctuate within a considerable range, and gradually decrease from 0.26 to 0.21 as the braking cycles increased. Whereas, the COF of C/C-Cu$_5$Si-TiC specimens slightly varied within the range from 0.18 to 0.16, suggesting more favorable braking stability than C/C-SiC. Note that the results in Fig. 8(c) are also consistent with the curves shown in Fig. 8(b). Therefore, it can be concluded that the infiltration with Cu-Ti alloy leads to a more stable friction behavior.

Fig. 9 shows the linear wear rate (LWR) of the C/C-SiC and C/C-Cu$_5$Si-TiC composites tested with different braking speeds. It is seen that the LWR of C/C-SiC composites decreases monotonically with increasing brake speed. Whereas, the LWR of C/C-Cu$_5$Si-TiC composites shows only a slight increase with increasing brake speed. Furthermore, the LWR of the C/C-Cu$_5$Si-TiC composites is much lower than that of C/C-SiC for all braking speeds. The maximum LWR of C/C-Cu$_5$Si-TiC composites in this work is merely 0.65 μm side^{-1} cycle^{-1}, while the minimum LWR of C/C-SiC is as high as 1.42 μm side^{-1} cycle^{-1}. In short, the wear resistance of C/C-SiC composites could be effectively enhanced after introducing the Cu-Ti alloy.

The morphology of typical friction surfaces for C/C-SiC and C/C-Cu$_5$Si-TiC specimens after several braking cycles is shown in Fig. 10. As shown in Fig. 10(a), after the 1st braking cycle, the grooves in the C/C region are clearly observed in the C/C-SiC specimens. However, no grooves in the SiC (gray phase) and Si (white phase) are observed because of their higher hardness. After the 20th braking cycle, the grooves in the C/C-SiC specimens evolve into a smoother surface (see Fig. 10(b)). According to the 3D profile of the sample after 20 braking cycles, shown in Fig. 10(c), the C/C and Si regions are seemingly smooth, whereas SiC micro-peaks are observed on the C/C-SiC surfaces. Due to its lower hardness, one can assume that the C/C and Si phases will deform by the shear and compressive stresses, and wear much faster than the SiC phase. As the braking cycles increase, the SiC phases as asperities on the surface will gradually gather debris and lead to an increasingly smooth surface. Therefore, the smooth friction surface is mainly the reason for the decreased COF of C/C-SiC as shown in Fig. 8(c). The C/C-Cu$_5$Si-TiC composites show a different friction surface (see Fig. 10(d)) due to its distinct microstructure. Cu$_5$Si, as a metallic phase, is of very lower hardness in comparison to the other carbides. Therefore, the deformation in Cu$_5$Si region is more likely to occur under the shear and compressive forces before the other regions. Nevertheless, this Cu$_5$Si matrix is reinforced with several TiC microparticles. Thus, the TiC particles will fill the grooves formed as the soft Cu$_5$Si matrix deforms. Therefore, the matrix develops into several small friction films between the carbon fibers, as seen for the friction surface after the first braking cycles in Fig. 10(d). With increasing braking cycles, the friction films enlarge and become smoother, as seen for the friction surface after 20 braking cycles in Fig. 10(e) and Fig. 10(f). As a consequence, the COF of the C/C-Cu$_5$Si-TiC specimen is lower, but much more stable, and the measured wear rates are also much smaller,

as seen in Figs. 8 and 9, respectively.

Fig. 11 presents the wear debris of C/C-SiC and C/C-Cu$_5$Si-TiC specimens after the braking tests. Both composites showed debris in the form of platelets, although differences can be seen in debris size and composition. As shown in Fig. 11(a), the debris from C/C-SiC composites is in the range of 200–500 μm. As presented in Fig. 11(c), the EDS analysis of the high-light region in Fig. 11(a) indicates that the debris is composed of Fe, O, C and Si elements. The oxides corresponding to FeO and Fe$_3$O$_4$ are originated from the oxidation of Fe element in 30CrSiMoVA counterpart during braking [32]. Compared to the debris from C/C-SiC specimens, the size of debris from C/C-Cu$_5$Si-TiC composites is bigger, ranging from 500 to 1000 μm (see Fig. 11(b)). The EDS shown in Fig. 11(d) indicates that the debris is mainly composed of Cu, Fe, Si, Ti and C. The Fe element within the debris is in the form of FeO and Fe$_3$O$_4$, ascribed to the wear of 30CrSiMoVA counterpart, while the Cu and Ti elements are ascribed to the wear of Cu$_5$Si and TiC, respectively.

Generally, the wear resistance and friction stability are related to the friction film and debris. The debris with considerable size is more likely to form continuous friction film, and result in stable friction behavior and low wear rate. During the braking, the Cu$_5$Si, softest phase, in C/C-Cu$_5$Si-TiC is easier to deform into friction film in comparison to C/C-SiC. Therefore, the improved friction characteristics of C/C-Cu$_5$Si-TiC composites are determined by friction film.

4. Conclusions

In order to improve the tribological performance, Cu-Ti alloy was successfully infiltrated into porous C/C-SiC materials via RMI process. Experimentally, the microstructure, physical properties and tribological behaviors of the as-processed C/C-Cu$_5$Si-TiC composites were characterized in comparison to C/C-SiC composites. Based on the performed investigations, following conclusions can be drawn:

(1) C/C-Cu$_5$Si-TiC composites were composed of carbon, Cu$_5$Si, TiC and traces of SiC without free Si. The microstructure consisted of Cu$_5$Si matrix reinforced by TiC particles and C$_f$/PyC units. The highest concentration of TiC and SiC were around the C$_f$/PyC, although the carbon fibers were well protected from the aggressiveness of liquids.
(2) As a result of the obtained microstructure, C/C-Cu$_5$Si-TiC composites possessed favorable thermal conductivity and mechanical properties. Compared to C/C-SiC specimens, the thermal diffusivity, flexural strength and impact toughness of the C/C-Cu$_5$Si-TiC composites with the same fiber architecture increased from 0.05 cm^2 s^{-1} to 0.08 cm^2 s^{-1}, 96 MPa to 110MPa, and 2.8 kJ m^{-2} to 7.9 kJ m^{-2}, respectively.
(3) Compared to the C/C-SiC composites, the C/C-Cu$_5$Si-TiC composites showed a significantly enhanced wear resistance. In summary, a decreased linear wear rate and higher frictional stability could be achieved in the C/C-Cu$_5$Si-TiC composites with the expense of lower coefficient of friction.
(4) In comparison to the C/C-SiC, the hardness of the C/C-Cu$_5$Si-TiC was significantly reduced due to the introduction of soft Cu$_5$Si phase. Nevertheless, the resultant microstructure allowed for the formation of bigger debris and continuous friction film. As a consequence, the new composite resulted in more stable friction behavior and lower wear rate.

Acknowledgement

References

[1] W. Krenkel, P. Schanz, Fiber ceramic structures based on liquid impregnation technique, Acta Astronaut. 28 (1992) 159–169.
[2] W. Krenkel, Carbon fiber reinforced CMC for high-performance structures, Int. J. Appl. Ceram. Technol. 1 (2004) 188–200.
[3] Y. Li, P. Xiao, Y. Shi, R.S.M. Almeida, W. Zhou, Z. Li, H. Luo, F. Reichert, N. Langhof, W. Krenkel, Mechanical behavior of LSI based C/C-SiC composites subjected to flexural loadings, Compos. Part A: Appl. Sci. Manuf. 95 (2017) 315–324.
[4] Y. Li, P. Xiao, H. Luo, R.S.M. Almeida, Z. Li, W. Zhou, A. Brückner, F. Reichert, N. Langhof, W. Krenkel, Fatigue behavior and residual strength evolution of 2.5D C/C-SiC composites, J. Eur. Ceram. Soc. 36 (2016) 3977–3985.
[5] Y. Li, P. Xiao, Z. Li, W. Zhou, T. Liensdorf, W. Freudenberg, N. Langhof, W. Krenkel, Tensile fatigue behavior of plain-weave reinforced Cf/C-SiC composites, Ceram. Int. 42 (2016) 6850–6857.
[6] W. Krenkel, F. Berndt, C/C-SiC composites for space applications and advanced friction systems, Mater. Sci. Eng.: A 412 (2005) 177–181.
[7] Z. Li, P. Xiao, X. Xiong, Microstructure and tribological properties of 3D needle-punched C/C-SiC brake composites, Solid State Sci. 12 (2010) 617–623.
[8] H. Abu El-Hija, W. Krenkel, S. Hugel, Development of C/C-SiC brake pads for high-performance elevators, Int. J. Appl. Ceram. Technol. 2 (2005) 105–113.
[9] Z. Li, Y. Long, Y. Li, J.-w. Li, X. Xiong, P. Xiao, Microstructure and properties of needle punching chopped carbon fiber reinforced carbon and silicon carbide dual matrix composite, Ceram. Int. 42 (2016) 9527–9537.
[10] Z. Li, P. Xiao, B.-g. Zhang, Y. Li, Y.-h. Lu, S.-h. Zhu, Preparation and dynamometer tests of 3D needle-punched C/C-SiC composites for high-speed and heavy-duty brake systems, Int. J. Appl. Ceram. Technol. 13 (2016) 423–433.
[11] S. Fan, L. Zhang, Y. Xu, L. Cheng, G. Tian, S. Ke, F. Xu, H. Liu, Microstructure and tribological properties of advanced carbon/silicon carbide aircraft brake materials, Compos. Sci. Technol. 68 (2008) 3002–3009.
[12] S. Fan, L. Zhang, L. Cheng, J. Zhang, S. Yang, H. Liu, Wear mechanisms of the C/SiC brake materials, Tribol. Int. 44 (2011) 25–28.
[13] Z. Li, P. Xiao, X. Xiong, B.-y. Huang, Preparation and tribological properties of C fibre reinforced C/SiC dual matrix composites fabrication by liquid silicon infiltration, Solid State Sci. 16 (2013) 6–12.
[14] X. Fan, X. Yin, Y. Ma, L. Zhang, L. Cheng, Oxidation behavior of C/SiC-Ti3SiC2 at 800–1300 °C in air, J. Eur. Ceram. Soc. 36 (2016) 2427–2433.
[15] S. Fan, Y. Du, L. He, C. Yang, H. Liu, L. Cheng, L. Zhang, N. Travitzky, Microstructure and properties of α-FeSi2 modified C/C-SiC brake composites, Tribol. Int. 102 (2016) 10–18.
[16] M. Esfehanian, J. Guenster, J.G. Heinrich, J. Horvath, D. Koch, G. Grathwohl, High-temperature mechanical behavior of carbon–silicide–carbide composites developed by alloyed melt infiltration, J. Eur. Ceram. Soc. 28 (2008) 1267–1274.
[17] M. Singh, D.R. Behrendt, Reactive melt infiltration of silicon-molybdenum alloys into microporous carbon preforms, Mater. Sci. Eng.: A 194 (1995) 193–200.
[18] H.-T. Fang, J.-H. Jeon, J.-C. Zhu, Z.-D. Yin, Inhibition of liquid Si infiltration into carbon–carbon composites by the addition of Al to the Si slurry pre-coating: mechanism analysis, Carbon 40 (2002) 2559–2565.
[19] Y. Tong, S. Bai, H. Zhang, K. Chen, C/C-SiC composite prepared by Si–10Zr alloyed melt infiltration, Ceram. Int. 38 (2012) 3301–3307.
[20] M. Esfehanian, J. Günster, F. Moztarzadeh, J.G. Heinrich, Development of a high temperature Cf/XSi2–SiC (X = Mo, Ti) composite via reactive melt infiltration, J. Eur. Ceram. Soc. 27 (2007) 1229–1235.
[21] Y. Wang, X. Zhu, L. Zhang, L. Cheng, C/C–SiC–ZrC composites fabricated by reactive melt infiltration with Si0.87Zr0.13 alloy, Ceram. Int. 38 (2012) 4337–4343.
[22] X. Fan, X. Yin, S. He, L. Zhang, L. Cheng, Friction and wear behaviors of C/C-SiC composites containing Ti3SiC2, Wear 274–275 (2012) 188–195.
[23] X. Fan, X. Yin, X. Cao, L. Chen, L. Cheng, L. Zhang, Improvement of the mechanical and thermophysical properties of C/SiC composites fabricated by liquid silicon infiltration, Compos. Sci. Technol. 115 (2015) 21–27.
[24] Z. Li, Y.-z. Liu, B.-g. Zhang, Y.-h. Lu, Y. Li, P. Xiao, Microstructure and tribological characteristics of needled C/C–SiC brake composites fabricated by simultaneous infiltration of molten Si and Cu, Tribol. Int. 93 (Part A) (2016) 220–228.
[25] R. Zhang, X. He, Z. Chen, X. Qu, Influence of Ti content on the microstructure and properties of graphite flake/Cu-Ti composites fabricated by vacuum hot pressing, Vacuum 141 (2017) 265–271.
[26] H. Okamoto, Cu-Si (copper-silicon), J. Phase Equilibria Diffus. 33 (2012) 415–416.
[27] B. Heidenreich, C/SiC and C/C-SiC Composites, Ceramic Matrix Composites, John Wiley & Sons, Inc., Hoboken, NJ, USA, 2014, pp. 147–216 http://onlinelibrary.wiley.com/doi/10.1002/9781118832998.ch6/summary.
[28] G.W. Liu, M.L. Muolo, F. Valenza, A. Passerone, Survey on wetting of SiC by molten metals, Ceram. Int. 36 (2010) 1177–1188.
[29] P. Gargarella, S. Pauly, M.F. de Oliveira, U. Kühn, J. Eckert, Glass formation in the Ti–Cu system with and without Si additions, J. Alloy. Compd. 618 (2015) 413–420.
[30] Z. Stadler, K. Krnel, T. Kosmac, Friction behavior of sintered metallic brake pads on a C/C–SiC composite brake disc, J. Eur. Ceram. Soc. 27 (2007) 1411–1417.
[31] L.M. Manocha, G. Prasad, S. Manocha, Carbon-ceramic composites for friction applications, Mech. Adv. Mater. Struct. 21 (2014) 172–180.
[32] J. Deng, N. Li, B. Zheng, S. Fan, L. He, C. Yang, H. Liu, L. Zhang, L. Cheng, Tribological behaviors of 3D needled C/C–SiC and FeSi75 modified C/C–SiC brake pair, Tribol. Lett. 65 (2017) 32.